

Full Length Article

Photocatalytic H₂ generation and CO₂ reduction by WB_{5-x} cocatalyst of TiO₂ catalyst

Anna Yu. Kurenkova ^{a,1}, Aleksandra D. Radina ^{b,1}, Viktor S. Baidyshev ^b, Pavel V. Povalyaev ^c, Egor E. Aidakov ^a, Evgeny Yu. Gerasimov ^a, Denis D. Mishchenko ^d, Angelina V. Zhurenok ^a, Alexander Ya. Pak ^c, Ekaterina A. Kozlova ^a, Alexander G. Kvashnin ^{b,e,*}

^a Boreskov Institute of Catalysis, Siberian Branch of the Russian Academy of Sciences, 5 prosp. Lavrent'eva, 630090 Novosibirsk, Russian Federation

^b Skolkovo Institute of Science and Technology, 121205, Bolshoi Blv. 30, Building 1, Moscow, Russian Federation

^c National Research Tomsk Polytechnic University, 30 Lenin Avenue, Tomsk 634050, Russian Federation

^d Synchrotron Radiation Facility SKIF, Boreskov Institute of Catalysis SB RAS, 630559 Koltsovo, Russian Federation

^e University of Science and Technology "MISIS", Leninsky prospekt 4, Moscow 119049, Russian Federation

A B S T R A C T

Catalytic reactions play an important role in modern industry as almost 90 % of the chemical industry is based on catalytic reactions. The development of new, more efficient catalysts will allow significant advances in chemical production, but still remains a rather challenging problem for materials scientists. Here, we have proposed and investigated a new composite photocatalyst based on WB_{5-x}WB₂ and TiO₂ for H₂ evolution from aqueous ethanol solution and CO₂ reduction under visible light irradiation (410 nm). New composite photocatalysts WB_{5-x}WB₂/TiO₂ were synthesized and characterized by X-ray diffraction, UV-vis spectroscopy, X-ray photoelectron spectroscopy, and high-resolution transmission electron microscopy. Photocatalytic measurements show that the maximum activity of the composite photocatalyst 4 and 23 times higher than the activity of unmodified TiO₂ in CO₂ reduction and H₂ evolution, respectively. Density functional calculations of the proposed reaction are in agreement with the provided experiments confirming the higher efficiency of the modified catalyst compared to TiO₂.

1. Introduction

Catalysts are compounds used in the chemical industry to change the rate of chemical reactions that are not present in the final products. Considering photocatalysis as a large part of heterogeneous catalysis, it is worth highlighting its main advantage – the ability to use light energy to obtain valuable compounds [1–3]. Using energy of light, it becomes possible to transform even thermodynamically stable molecules such as carbon dioxide [4–6]. The products of CO₂ reduction are hydrocarbons and alcohols, which can be used to produce synthetic fuels [7–10]. Thus, photocatalysis enables the use of CO₂ obtained from the combustion of fossil fuels to produce new energy sources. This contributes to solving two problems at the same time: the rapidly increasing concentration of CO₂ in the atmosphere and the reduction of reserves of traditional fuels.

Another promising direction in the development of photocatalytic technologies is the production of hydrogen from aqueous solutions. Unlike industrial methods of hydrogen production, this process can only use renewable resources – water and solar irradiation [11,12]. It should be noted that both reactions - the photocatalytic conversion of carbon

dioxide and the production of hydrogen - take place at room temperature and atmospheric pressure, which significantly reduces the costs for the processes [13,14]. Since the process of decomposing pure water into hydrogen and oxygen is kinetically rather difficult, electron donors are added to the system – substances that react with photogenerated holes [15]. Various organic and inorganic compounds, including alcohols, sugars, sodium sulfide, etc. are used as electron donors [16]. Ethanol can be obtained from the fermentation of sugars, making it a renewable resource, which is attractive from the point of view of developing alternative energy sources[17].

The most widely used photocatalyst for these purposes is titanium dioxide TiO₂ due to its stability, availability, and lack of toxicity [18,19]. However, it is important to note that the anatase modification has a band gap of 3.3 eV, whereas the rutile modification has a band gap of 3.0 eV. As a result, activation of TiO₂ requires ultraviolet (UV) irradiation [20,21]. Nevertheless, as only a small fraction of the solar spectrum is UV, it is crucial to modify TiO₂ to activate it under visible light, which accounts for approximately 46 % of the solar spectrum [22]. In addition, the position of the TiO₂ conduction band is close to 0 vs.

* Corresponding author.

E-mail address: A.Kvashnin@skoltech.ru (A.G. Kvashnin).

¹ These authors contributed equally

NHE, resulting in a low reduction capability of photogenerated electrons [23]. In order to increase the activity of TiO_2 , a large number of modification methods are used, among which the deposition of noble metals, especially platinum, on the surface of TiO_2 is considered to be the most effective. Unfortunately, this method of modification results in a considerable rise in the cost of the photocatalyst. As a result, extensive research has been carried out to identify a substitute cocatalyst that can effectively modify TiO_2 for various photocatalytic processes under visible light irradiation in order to reduce the costs involved.

As an alternative to noble metal cocatalysts, one can potentially consider transition metals or compounds based on them, such as carbides [24,25] or borides [26–29]. The catalytic activity of transition metal borides (TMBs) is explained by the influence of transition metals in their composition [29], but the contribution of the boron sublattice to H_2 evolution reaction or CO_2 conversion is still under debate [30]. Furthermore, it has been shown previously [29,30] that catalytic activity of TMBs depends on a stoichiometric ratio between boron and metal in the compound. In the case of molybdenum borides catalytic activity increases as the boron content in the compound increases [31]. The less active compound is Mo_2B which has isolated boron atoms in a metallic sublattice. Li et al. [29] showed that WB_3 is the most efficient of all the examined tungsten borides, with a lower energy for HER than platinum catalysts used in organic synthesis [32,33].

As most metal borides are metals in terms of electronic properties [34] it is possible to consider their utilization as cocatalysts supported by the main catalyst (i.e. TiO_2) for different photocatalytic reactions including CO_2 reduction [35,36] and hydrogen production from various solutions [37,38]. The absence of band gap allows the transfer of "hot electrons" between the cocatalyst and the TiO_2 catalyst, which significantly increases the yield of photocatalytic reactions.

Here we proposed the composite photocatalyst of higher tungsten boride $\text{WB}_{5-x}\text{-WB}_2$ powder supported on TiO_2 substrate for H_2 generation from aqueous ethanol solutions and CO_2 reduction under visible light irradiation. Our study shows that the presence of WB_{5-x} nanopowder significantly increases the reaction yield compared to pure semiconducting TiO_2 . Density functional calculations show lower energy barriers of H_2 generation for the reaction occurring on WB_{5-x} surfaces compared to TiO_2 , confirming the experimental observations.

2. Materials and methods

2.1. Synthesis of $\text{WB}_{5-x}\text{-WB}_2$ powder

Synthesis of powder of higher tungsten borides was realized using the vacuumless electric arc method [39]. The process is based on the high-temperature treatment of graphite crucibles by atmospheric electric discharge plasma, in which a pre-prepared mixture of tungsten and boron powders is placed. During the arc-discharge combustion, two main physical phenomena are realized which ensure the synthesis: (i) release of thermal energy leading to the approach of the temperature sufficient for the interaction of boron with tungsten; (ii) oxidation of the graphite elements of the discharge circuit by oxygen from the air with the formation of an autonomous gaseous environment consisting of CO and CO_2 . This method has already been successfully used for the synthesis of high-entropy carbides [40], and higher tungsten boride ($\text{WB}_{5-x}\text{-WB}_2$) [39].

In contrast to previous work, an improved arc reactor was used, which significantly increased the working volume of the reaction zone and minimized carbon contamination caused by anode erosion. Figure S1 in the Supporting Information shows a simplified diagram of the reactor. The reactor is powered by a rectifier-inverter converter, which can regulate the current up to 200 A. Copper wires from the power source are fixed on current-carrying electrode holders with at least 99.9 % purity of carbon electrode from QiJing Trading Co. (made in China). A graphite cylindrical rod with a diameter of 8 mm and length of 100 mm was connected to the power source's positive terminal. The

negative terminal of the power source was connected to an aluminum plate on which a graphite crucible is mounted. The crucible measures 30 mm in diameter and 40 mm in height. A smaller graphite crucible, measuring 20 mm in diameter and height, was placed inside the graphite crucible that was already installed on the aluminum plate. The initial mixture was loaded into the cavity. Once the initial mixture is added, the crucible is then covered with a graphite cover that serves as a contact pad to start arc discharge. By doing this, any carbon impurities formed from erosion of the graphite elements in the system are prevented from entering.

A linear electric drive operated by the controller was used to move the anode in the crucible cavity until it made contact with the graphite cover of the small crucible. The anode was moved in the cavity of the graphite crucible and made contact with the graphite cover after the power source was switched on and the actuator was activated. Once discharge between the rod and the small crucible lid was initiated, the rod was moved to the specified discharge gap of almost 1 mm and held for the set time.

A small graphite crucible filled with a mixture of tungsten and boron powders in the atomic ratio $\text{W:B} = 1:15$ (determined previously [39] to be optimal) with a mass of up to 5 g was treated with electric arc plasma at a current of 200 A with dwell time of 60 s.

2.2. Preparation of $\text{WB}_{5-x}\text{-WB}_2/\text{TiO}_2$ photocatalysts

To prepare photocatalysts with 1, 5, 10, and 20 wt% of higher tungsten boride, the required quantities of synthesized $\text{WB}_{5-x}\text{-WB}_2$ powder and commercial TiO_2 Evonik P25 were mixed in 50 mL of acetone. The mixture was sonicated for 15 min and stirred for 1 h. The resulting mixture was then heated in a water bath at 80 °C for 1 h, washed several times with distilled water and finally dried in an oven at 60 °C for 12 h.

2.3. Photocatalyst characterization

The photocatalysts that were prepared underwent characterization using scanning electron microscopy (SEM), high-resolution transmission electron microscopy (HR TEM), X-ray diffraction (XRD), X-ray photo-electron spectroscopy (XPS), and diffuse reflectance spectroscopy in UV-vis region.

The structure and microstructure of the catalyst were examined using HR TEM with a ThemisZ electron microscope (Thermo Fisher Scientific, USA), which operates at a 200 kV accelerating voltage. The microscope boasts a spherical aberration corrector affording a maximum lattice resolution of 0.06 nm and a SuperX energy-dispersive spectrometer (Thermo Fisher Scientific). Ceta 16 CCD sensor (Thermo Fisher Scientific) was employed to capture images. For the purpose of electron microscopy investigations, specimens were placed onto perforated carbon supports fixed to aluminum grids utilizing an ultrasonic disperser. The morphology of $\text{WB}_{5-x}\text{-WB}_2$ particles was studied by SEM with a Tescan Solaris electron microscope (Tescan, Czech) equipped with secondary electron (in-beam SE) detector and back-scattered electron detector (in-beam f-BSE). Energy-dispersive spectroscopy analysis was made using OXFORD Aztec spectrometer.

X-ray diffraction patterns were obtained using a Bruker D8 Advance diffractometer ($\text{Cu K}\alpha$ Ni-filtered radiation, $\lambda = 1.5418 \text{ \AA}$), which was equipped with a Lynxeye linear detector (Bruker AXS GmbH, Germany). The diffraction patterns were collected in the 2θ range of 23 to 77° for $\text{WB}_{5-x}\text{-WB}_2/\text{TiO}_2$ samples and in the 2θ range of 23 to 74.5° for $\text{WB}_{5-x}\text{-WB}_2$ samples with a step of 0.02°. Rietveld refinement was performed for each XRD pattern using GSAS-II software packages [41].

The chemical state of cations and surface composition of the catalyst were studied via XPS using a photoelectron spectrometer (SPECS Surface Nano Analysis GmbH, Berlin, Germany) using non-monochromatized $\text{Al K}\alpha$ radiation ($\hbar\nu = 1486.6 \text{ eV}$). The spectrometer was equipped with a PHOIBOS-150 hemispherical analyzer and an XR-

50 X-ray source with a double Al/Mg anode. The calibration of the binding energy scale was performed by setting the W 4f_{7/2} peak of tungsten corresponding to tungsten in the W⁶⁺ state at 36.1 eV and the Ti 2p_{3/2} peak of the TiO₂ at 459 eV.

The diffuse reflectance spectra in the 300–700 nm region were obtained with a UV-2501 PC spectrophotometer with an ISR-240A diffuse reflectance unit (Shimadzu, Kyoto, Japan).

2.4. Experimental setup

The photocatalytic activity of the synthesized samples was tested in the photocatalytic H₂ evolution reaction (HER) from water solution and in the photocatalytic CO₂ reduction reaction (CO₂ RR) in the gas phase under visible light irradiation.

To measure the activity of photocatalysts in the hydrogen evolution reaction, 50 ml of a 10 % aqueous ethanol solution and 25 mg of a photocatalyst were placed in the reactor ($V = 207 \text{ mL}$) with a quartz window ($S = 28.3 \text{ cm}^2$). The stirring speed was set to 500 rpm on the magnetic stirrer. The reactor was purged with argon for 30 min and then irradiated with a LED with a maximum intensity at a wavelength of 410 nm (Fig. S2a in the Supporting Information), the power density was 70 mW·cm⁻². The scheme of set-up for the photocatalytic H₂ evolution experiment is shown in Fig. S2b in the Supporting Information.

To determine the activity of the photocatalyst in the CO₂ reduction reaction, a suspension was prepared consisting of a photocatalyst (30 mg) and about 500 μL of ultrapure water ("NuZar Q" water system set). Then the resulting suspension was deposited to glass support (8 cm^2) and dried in air at 60 °C for 30 min. After that, the photocatalyst was kept for 30 min under UV irradiation (365 nm) in air to remove organic impurities from the surface of the photocatalyst. Then the glass support with a photocatalyst was placed on a Teflon stand in a reactor ($V = 170 \text{ mL}$) containing 1 mL of ultrapure water and purged with CO₂ (99.995 %) for 1 h. The 1 mL of water required to form saturated water vapor is added to the bottom of the reactor so that the photocatalyst is in contact only with the water vapor and not with the liquid. The same diode (410 nm, 70 mW·cm⁻²) was used as the light source, the distance from the glass support with a photocatalyst is 7 cm. A detailed scheme of the set-up for the photocatalytic CO₂ reduction is given in our previous work [42].

Gas probe was analyzed with a gas chromatograph "GH-1000" (Chromos, Russia) equipped with the flame ionization detector and thermal conductivity detector to identify the products of CO₂ reduction and H₂, respectively. The rate of electron consumed W_e during photocatalytic CO₂ reduction (CO₂ RR) based on electron balance was calculated according to the following equation:

$$W_e - (\text{CO}_2\text{RR}) = 8W(\text{CH}_4) + 2W(\text{CO}) \quad (1)$$

where $W(\text{CH}_4)$ and $W(\text{CO})$ are the production rate of CH₄ and CO ($\mu\text{mol h}^{-1} \text{ g}_{\text{cat}}^{-1}$), 2 and 8 are the coefficients for electron balance. The experimental error in determining the reaction rate, calculated based on a series of experiments, is no more than 10 %.

2.5. Computational details

The WB_{5-x} slabs with (010) and (101) surfaces and anatase TiO₂ slab with (101) surface were generated from the relaxed bulk structures using the atomic simulation environment (ASE) [43]. We have used the model of bulk WB_{5-x} from Ref. [44] to construct the slabs. The structure of anatase TiO₂ was taken from MaterialProject [45]. We consider the (101) surface of anatase TiO₂, which is considered the most thermodynamically stable [46]. The thickness of obtained slabs varied from 8 to 12 Å depending on the surface orientation.

Relaxation of geometry of the slabs, calculations of electronic density of states together with electronic band structure were performed by using density functional theory (DFT) as implemented in VASP [47–49]

package. The exchange–correlation effects were treated using the generalized gradient approximation (GGA) with the Perdew-Burke-Ernzerhof (PBE) parametrization [50]. The projector augmented-wave (PAW) method [51] was used to describe the interactions between the ionic core and valence electrons. The cutoff energy of plane waves was set to 500 eV. The partition of the first Brillouin zone into a grid of k-points was carried out within the Monkhorst–Pack scheme [52] with a resolution of $2\pi \times 0.05 \text{ \AA}^{-1}$. A vacuum region of 25 Å perpendicular to each surface was used to avoid the artificial interactions between periodic images of the slabs.

To consider strong electron correlations between the localized 3d-electrons of Ti atoms, the GGA + U approach in Dudarev's formulation [53,54] was applied, where the values of parameter $U_{\text{eff}} = U - J$ were taken to be $U = 9.25 \text{ eV}$ and $J = 1 \text{ eV}$ [55] ensuring the correct band gap value of bulk anatase TiO₂ of 3.16 eV (experimental value is 3.2 eV [56]). Calculated electronic densities of states of bulk TiO₂ and WB_{5-x} are shown in Figure S3 in the Supporting Information.

Adsorption energies of ethanol molecules on the WB_{5-x} and TiO₂ surfaces were calculated by using spin-polarized generalized gradient approximation (GGA) with the PBE parametrization [50]. The Grimme corrections (DFT-D3) [57] were applied to take into account van der Waals interaction between considered surfaces and ethanol molecules.

Different configurations of ethanol molecule on the considered surfaces were examined to find those with lowest adsorption energy. All the analyzed configurations are provided in Figure S4 in the Supporting Information. Accordingly, the adsorption energy for each molecule configuration on the adsorption site was calculated using the subsequent equation:

$$E_{\text{ads}} = E_{\text{calc}} - E_{\text{slab}} - E_{\text{ethanol}} \quad (2)$$

where E_{calc} is the energy of the slab with adsorbed molecules, E_{slab} is the energy of the pure substrate, E_{ethanol} is the energy of the ethanol molecule. The activation energies for considered hydrogen production reactions from ethanol molecules were obtained using the climbing image nudged elastic band method (CI-NEB) [58].

3. Results and discussions

3.1. Photocatalyst characterization

To ensure that the WB_{5-x}-WB₂ powder was successfully deposited on the TiO₂ surface XRD measurements were performed on the prepared samples. The X-ray diffraction patterns of TiO₂ coated with WB_{5-x}-WB₂ powder of 1, 5, 10, and 20 wt%, are as shown in Fig. 1. XRD patterns of two polymorphic modifications of TiO₂ (Fig. 1a) were simulated to define the presence of TiO₂ structure on studied composites. The main reflections of the TiO₂ XRD patterns are indicated by red and blue circles corresponding to rutile and anatase modifications. Fig. 1b shows the experimentally measured XRD pattern of TiO₂. Our simulations are in good agreement with the experimental measurements for TiO₂. Fig. 1c shows simulated XRD patterns of bulk WB₂ and WB_{5-x} as the main part of our cocatalyst. The measured XRD pattern of unsupported WB_{5-x}-WB₂ powder is shown in Fig. 1d, where reflections corresponding to WB₂ and WB_{5-x} compounds are indicated by open blue diamonds and open red triangles. The experimentally measured XRD pattern of the WB_{5-x}-WB₂ powder agrees well with the previously reported patterns from refs. [40,44]. Both WB₂ and WB_{5-x} have hexagonal structures (space group $P6_3/mmc$). The addition of 1 wt% of WB_{5-x}-WB₂ does not alter the XRD pattern of the TiO₂ substrate, as shown in Fig. 1e. Only reflections corresponding to anatase and rutile TiO₂ are observed. Increasing the amount of higher tungsten boride leads to the appearance of reflections related to WB_{5-x} and WB₂ structures, as shown in Fig. 1f-h for 5, 10, and 20 wt%. As the amount of WB_{5-x}-WB₂ powder increases, the intensity of the main reflections associated with WB_{5-x}-WB₂ powder also increases. Therefore, it can be conclude that the WB_{5-x}-WB₂ powder is located on

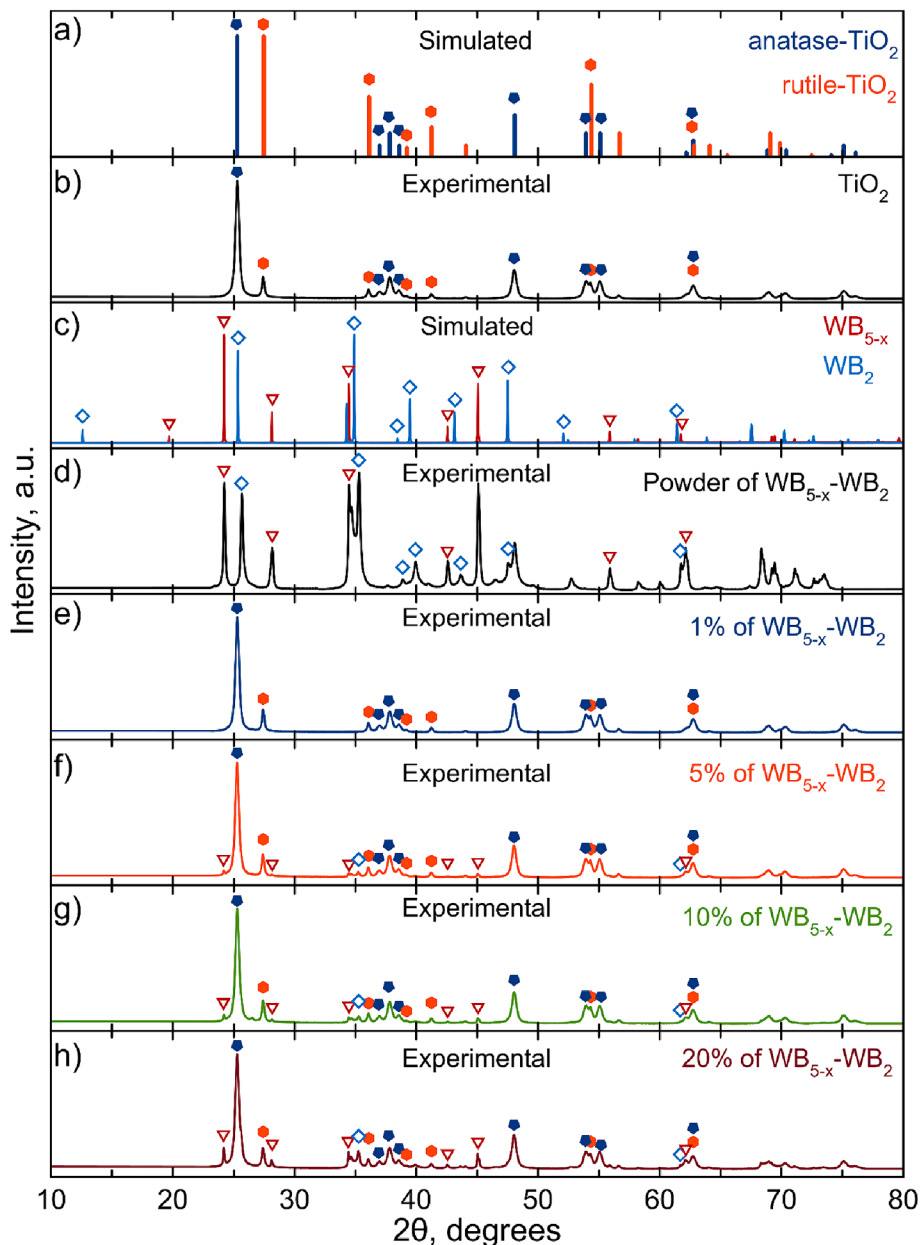


Fig. 1. Simulated and measured XRD patterns of studied materials. a) Simulated and b) measured XRD patterns of anatase and rutile polymorphic modifications of TiO_2 . c) Simulated XRD patterns of WB_{5-x} and WB_2 structures. Measured XRD patterns of d) pure $\text{WB}_{5-x}\text{-}\text{WB}_2$ powder and $\text{WB}_{5-x}\text{-}\text{WB}_2\text{/TiO}_2$ composite catalyst with e) 1 wt%, f) 5 wt%, g) 10 wt%, and h) 20 wt% of $\text{WB}_{5-x}\text{-}\text{WB}_2$ placed on the TiO_2 substrate.

the TiO_2 substrate and does not flue away during the preparation of the $\text{WB}_{5-x}\text{-}\text{WB}_2\text{/TiO}_2$ composite. Furthermore, the increase in the amount of $\text{WB}_{5-x}\text{-}\text{WB}_2$ powder is clearly evident from the acquired XRD patterns.

Based on XRD data, we determined the relative phase content and crystallite size for WB_{5-x} and WB_2 for unmodified $\text{WB}_{5-x}\text{-}\text{WB}_2$ and (5, 10, and 20) % $\text{WB}_{5-x}\text{-}\text{WB}_2\text{/TiO}_2$ (Table 1). The titanium dioxide consists of anatase (86 wt%) and rutile (14 wt%) phases with average particle sizes of 34 and 48 nm, respectively. The synthesized tungsten boride is present in two phases WB_2 (60 wt%) and WB_{5-x} (40 wt%) with average particle sizes of 58 and 102 nm, respectively. Both phases belong to the $P6_3/mmc$ structure. In the composite catalysts, the predominance of the WB_2 phase content over the WB_{5-x} phase is maintained. The discrepancy between the calculated content of tungsten boride phases and that determined from the XRD data can be explained by the poor crystallinity of the synthesized tungsten boride samples, as well as the partial shielding of the tungsten boride phases by TiO_2 phases. Also, the

Table 1

Composition and coherent scattering region (CSR) of the co-catalyst according to XRD data.

| Photocatalyst | WB ₂ , wt.% | CSR (WB ₂), nm | WB _{5-x} , wt.-% | CSR (WB _{5-x}), nm |
|--|------------------------|----------------------------|---------------------------|------------------------------|
| 5 % $\text{WB}_{5-x}\text{-}\text{WB}_2\text{/TiO}_2$ | 1.3 ± 0.4 | 58 ± 5 | 0.6 ± 0.2 | 103 ± 9 |
| 10 % $\text{WB}_{5-x}\text{-}\text{WB}_2\text{/TiO}_2$ | 2.0 ± 0.5 | 50 ± 3 | 0.9 ± 0.4 | 95 ± 15 |
| 20 % $\text{WB}_{5-x}\text{-}\text{WB}_2\text{/TiO}_2$ | 5 ± 1 | 50 ± 2 | 3 ± 1 | 135 ± 17 |
| 100 % $\text{WB}_{5-x}\text{-}\text{WB}_2$ | 60 ± 1 | 52 ± 2 | 40 ± 1 | 78 ± 2 |

presence of large particles of amorphous B_2O_3 , whose content increases in composite photocatalysts (XPS results below) makes it difficult to determine the tungsten boride content.

The state of the elements in the surface layer of the photocatalysts was studied using the XPS method. Fig. 2 shows the W4f and W4d spectra of the studied samples. It is well known that the 4f-level of tungsten is split into two sublevels W4f_{7/2} and W4f_{5/2} due to spin-orbit interaction, the spin-orbit splitting of which is 2.2 eV. According to literature data for W⁰, W²⁺, W⁴⁺, W⁵⁺ and W⁶⁺, the binding energies of W4f_{7/2} are in the ranges 30.8–31.1, 31.6–31.9, 32.5–33.4, 33.5–34.8 and 35.5–36.1 eV, respectively [39,59–63].

In the W4f spectrum of the initial WB_{5-x}-WB₂ sample, three doublets W 4f_{7/2}-W4f_{5/2} with binding energies W4f_{7/2} around 36.1, 34.7 and 31.9 eV are observed in the W 4f spectrum, corresponding to tungsten in the W⁶⁺, W⁵⁺ and W⁴⁺ states, respectively. Comparing the results obtained with the data presented in Ref. [39], it is possible to relate the W⁶⁺ and W⁴⁺ states to WO₃ and WO₂ oxides, respectively.

However, for composite photocatalysts WB_{5-x}-WB₂/TiO₂, the spectrum of W4f overlaps with the spectrum of Ti3p (37.3 eV). At the same time, the concentration of tungsten relative to titanium in composite photocatalysts is low, resulting in low intensities of peaks related to tungsten. Therefore, the study of WB_{5-x}-WB₂/TiO₂ samples was carried out using the spectrum of tungsten W4d. The spectra in this region are also shown in Fig. 2b. It is known from the literature that the 4d level of tungsten is split into two sublevels W4d_{5/2} and W4d_{3/2} by spin-orbit interaction, the spin-orbit splitting of which is 12.6 eV. The binding energy of the W4d_{5/2} peaks of these two states is 246.2 eV for W⁵⁺ and 247.7 eV for W⁶⁺ [59–63], which are identified in the spectra of composite photocatalysts. The spectrum of unmodified WB_{5-x}-WB₂ also shows a low intensity peak of the W⁴⁺ state.

Fig. 2b shows the B1s spectra of the analyzed samples. For the initial WB_{5-x}-WB₂ sample, the B1s spectrum is accurately represented by four peaks with binding energies at approximately 187.3, 189.1, 190.6 and 192.9 eV, corresponding to the B-W, B-C, B-N and B-O bonds [39,64–66]. Literature data suggest that the peaks in the 192–194 eV range are due to B in B₂O₃. In the case of WB_{5-x}-WB₂/TiO₂ samples, an intense peak is observed in the B1s spectrum at 192.4–192.5 eV. This peak can be attributed to the B-O bond in the B₂O₃. In addition, three peaks of low intensity are observed, which are related to the B-N, B-C, and B-W bonds. The absence of B₂O₃ by XRD indicates that an amorphous phase of boron oxide is formed on the surface of the tungsten borides due to contact with atmospheric oxygen.

The O1s and C1s spectrum of the samples are shown in Figure S5 in the Supporting Information. The O1s spectra can be decomposed into three peaks. The peak with a binding energy around 529.8 eV refers to oxygen in TiO₂ [67], the second and third peaks with binding energies around 531.8 eV and 532.2 eV refer to surface oxygen in various impurities such as hydrocarbons, carboxyl or carbonate groups and boron oxide [68,69]. The C1s spectra of the samples can be decomposed into four peaks. The main C1s peak with a binding energy around 284.8, corresponds to hydrocarbon impurities with a predominance of C-C and C-H bonds. Amorphous carbon also has a similar binding energy value. The peaks with binding energies in the range of 286.3–286.5 eV region belong to carbon bound to oxygen and nitrogen [70,71]. Other peaks in the 288.8–288.9 eV region correspond to carboxyl or carbonate groups [72,73]. In addition, a C1s spectra show a peak with the C1s binding energy in the region of 282.8–283.0 eV. This carbon is a constituent of boron carbide BC_x [65,66,74]. The energies and ratios of the boron, oxygen and carbon forms in the initial WB_{5-x}-WB₂ sample and composite photocatalysts (1–20)% WB_{5-x}-WB₂/TiO₂ are presented in Table S1 in the Supporting Information.

The morphology of the synthesized WB_{5-x}-WB₂ particles was studied by scanning electron microscopy (SEM) (Fig. 3). Using two detectors with different sensitivity to phase structure and depth of analysis, it was found that the surface of the particles is coated with boron oxide (Fig. 3a), while the core contains tungsten borides (Fig. 3b). The EDX mapping shown in Fig. 3c, d demonstrates that oxygen-rich areas coincide with boron-rich areas, confirming the presence of boron oxide on the surface.

High-resolution transmission electron microscopy (HR TEM) was used to study the microstructure of the 5 % WB_{5-x}-WB₂/TiO₂ photocatalyst. The TiO₂ particles with well-crystallized surfaces are coated with tungsten borides, as shown in Fig. 4a–c. Analysis of the interplanar distances measured from the high-resolution images reveals the presence of non-stoichiometric WB_{5-x} and WB₂ phases of tungsten borides. The uniform distribution of WB_{5-x}-WB₂ over the TiO₂ surface is shown by EDX mapping, as shown in Fig. 3d.

To investigate the optical properties of the photocatalysts, diffuse reflectance spectra of unmodified TiO₂, WB_{5-x}-WB₂, and composite WB_{5-x}-WB₂/TiO₂ samples were obtained (Fig. S5a in the Supporting Information). Titanium dioxide has an absorption edge in the region of 380

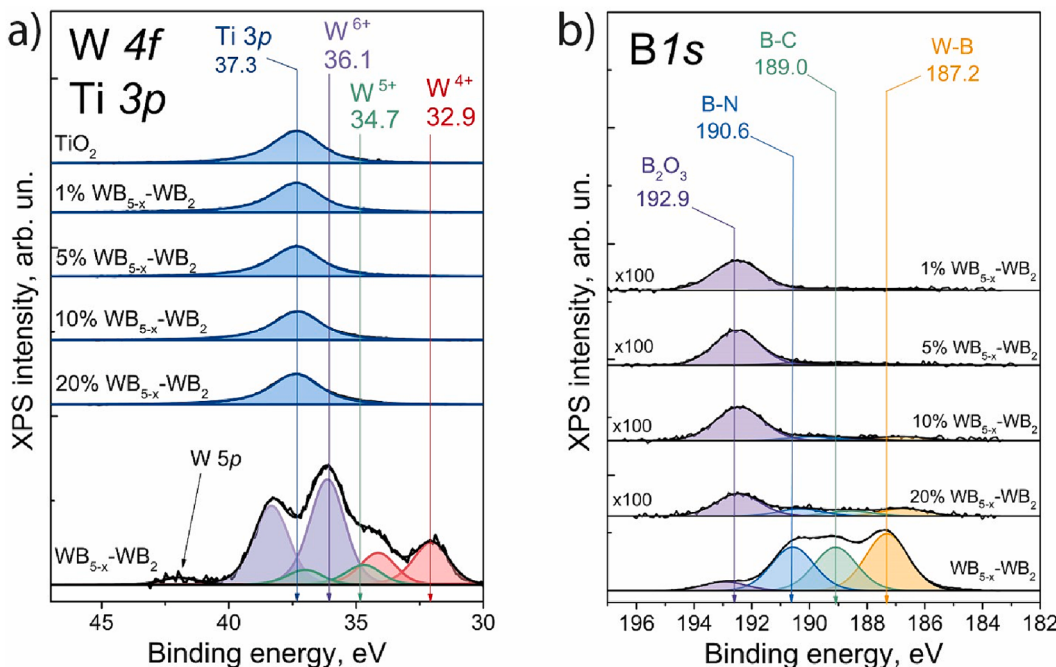


Fig. 2. W4f and Ti3p (a), B1s (b) core-level spectra of the initial WB_{5-x}-WB₂ sample and composite photocatalysts (1–20)% WB_{5-x}-WB₂/TiO₂.

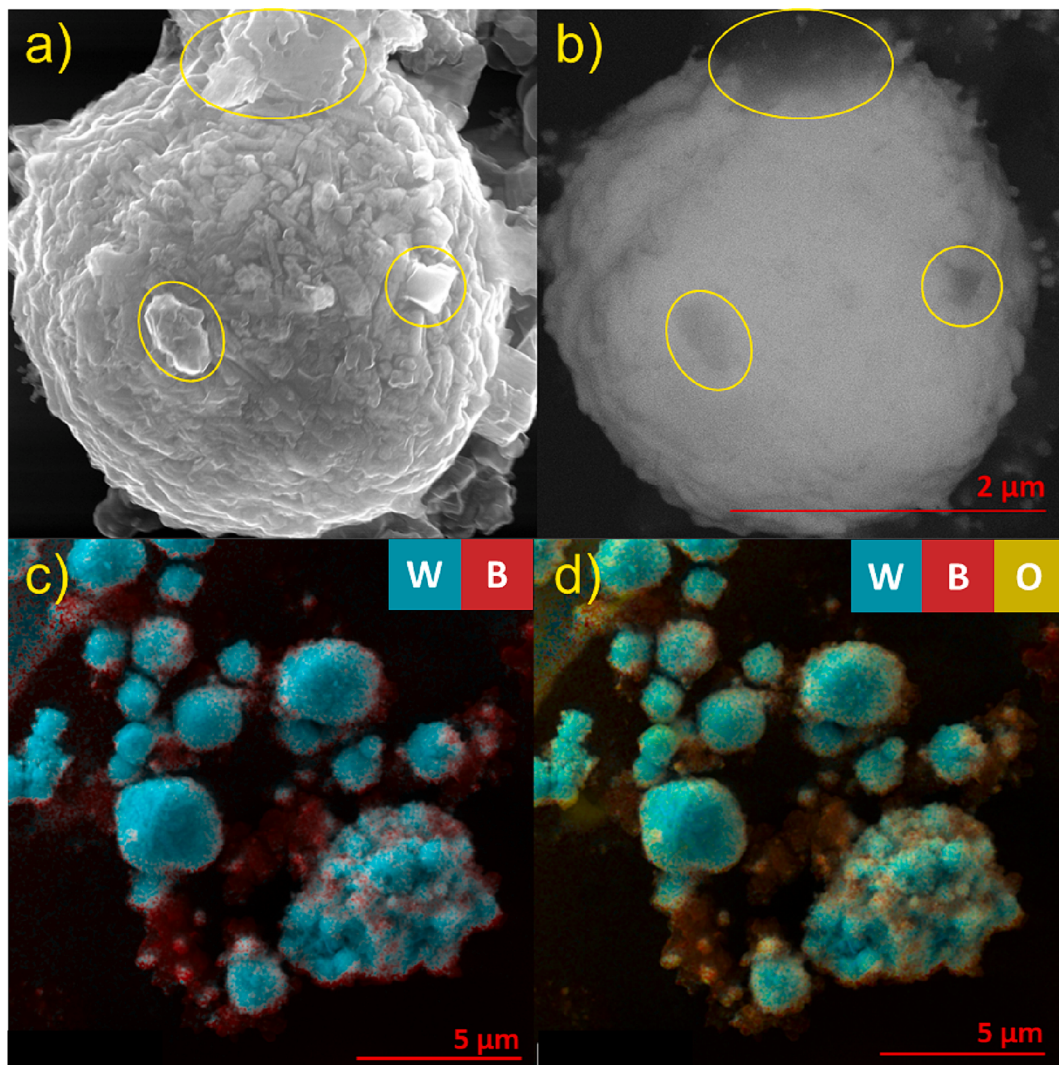


Fig. 3. SEM images of the synthesized $\text{WB}_{5-x}\text{-WB}_2$ particles. (a) Boron oxide particles (some circled in yellow) on the surface of $\text{WB}_{5-x}\text{-WB}_2$ (in-beam SE detector); (b) $\text{WB}_{5-x}\text{-WB}_2$ in the core of the particle (in-beam f-BSE detector); (c) and (d) EDX mapping of the synthesized $\text{WB}_{5-x}\text{-WB}_2$ particles. (For interpretation of the references to colour in this figure legend, the reader is referred to the web version of this article.)

nm, which is in agreement with the literature data [75]. The sample of $\text{WB}_{5-x}\text{-WB}_2$ shows absorption over the whole measuring range, indicating some similarity with the optical properties of metals. The deposition of $\text{WB}_{5-x}\text{-WB}_2$ on the TiO_2 surface leads to an increase in the absorption of the composite catalyst in the visible region, and the absorption increases with increasing $\text{WB}_{5-x}\text{-WB}_2$ content. The bandgap energies of the TiO_2 and composite photocatalysts are shown in Fig. S6b in the Supporting Information.

Using a combination of physicochemical methods, we have determined the composition and structure of the initial tungsten borides, titanium dioxide, and composite photocatalysts based on them. The initial tungsten borides consist of WB_{5-x} and WB_2 crystalline phases with amorphous B_2O_3 particles on the surface. The content of WB_2 phase predominates over the WB_{5-x} phase, and a similar ratio is observed in $\text{WB}_{5-x}\text{-WB}_2/\text{TiO}_2$ composite photocatalysts. In composite photocatalysts, the content of amorphous B_2O_3 phase increases compared to the initial tungsten borides. Elongated particles of WB_{5-x} and WB_2 are uniformly distributed on the surface of well-crystallized TiO_2 particles. The presence of relatively large particles of amorphous boron oxide (up to 1 μm) on the surface of the tungsten borides makes it difficult to determine the tungsten boride content in composite photocatalysts, which leads to the underestimation of the tungsten boride content by the XRD technique. Due to the relatively simple method of synthesising

composite photocatalysts, the content of the cocatalyst cannot be very different from that determined during synthesis. Based on the above, the cocatalyst content in composite photocatalysts is assumed to be close to the calculated value.

3.2. Electronic structure calculation

Since we have considered higher tungsten boride as a cocatalyst for TiO_2 , it is important to analyze its electronic structure and electronic band alignment with respect to the electronic bands of TiO_2 . We have calculated the electronic band structure, vacuum level, and Fermi energy for (010)- WB_{5-x} , (101)- WB_{5-x} , and (101)- TiO_2 slabs, together with isolated ethanol molecule as shown in Fig. 5. All energies were plotted with respect to the vacuum level. The energies of vacuum calculated for (010)- WB_{5-x} , (101)- WB_{5-x} , (101)- TiO_2 , and isolated ethanol molecule are 5.936, 6.192, 2.648, and -0.008 eV respectively. As can be seen, both surfaces of WB_{5-x} exhibit the absence of band gap, see Fig. 5a,b. The Fermi energy of (101)- TiO_2 shifts towards the conduction band compared to bulk TiO_2 due to the presence of surface states located in the band gap between -3 and -2 eV, see Fig. 5c, while the Fermi energy is -2.25 eV. This indicates a significant reduction of the band gap compared to the bulk. It should also be noted that the Fermi energy of (101)- WB_{5-x} is located above the valence band maximum of (101)- TiO_2 .

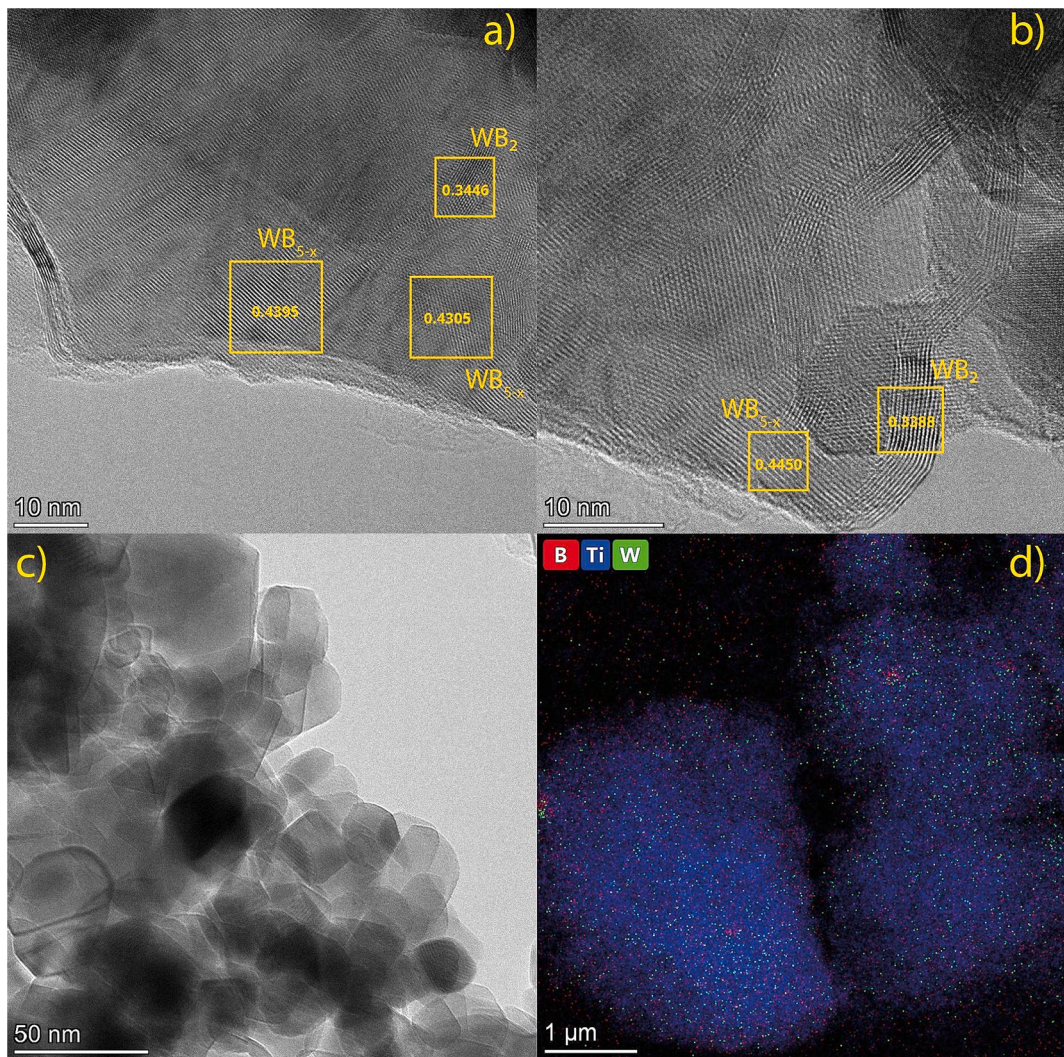


Fig. 4. HRTEM images (a-c) and EDX mapping (d) of 5% $\text{WB}_{5-x}\text{-WB}_2/\text{TiO}_2$ photocatalyst.

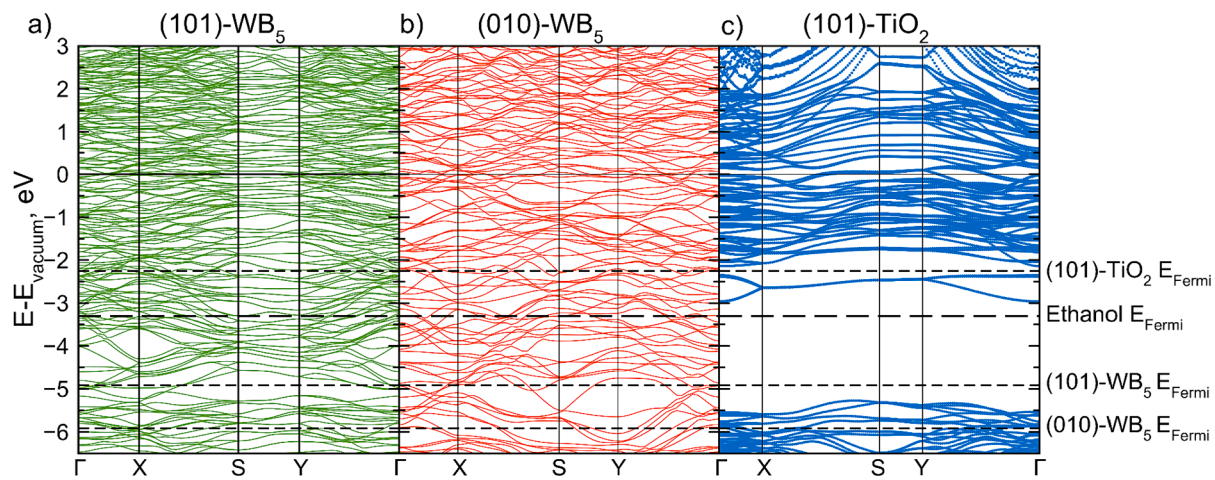


Fig. 5. Electronic bands of a) (101)- WB_{5-x} , b) (010)- WB_{5-x} , and c) (101)- TiO_2 calculated slabs with respect to the vacuum level. Bold dashed line represents the Fermi energy of an ethanol molecule, dashed lines represent the Fermi energies of considered slabs.

(−4.93 eV). This supports the electron transfer from the cocatalyst particles to the TiO_2 allowing the transfer of "hot electrons".

3.3. Adsorption and activation energy calculations

In order to study the adsorption of the ethanol molecule on the surfaces of TiO_2 and WB_{5-x} , we analyzed various configurations of

ethanol on selected surfaces: specifically, (101)-TiO₂, (010)-WB_{5-x}, and (101)-WB_{5-x}. Five different configurations of ethanol were considered on the (101)-TiO₂ surface, while four and five were selected and considered for (010)-WB_{5-x}, and (101)-WB_{5-x} respectively. Considered configurations together with calculated adsorption energies are shown in Figure S4 in the Supporting Information. The lowest adsorption energies of ethanol on (101)-TiO₂, (010)-WB_{5-x}, and (101)-WB_{5-x} are found to be -1.344, -1.310, and -1.496 eV respectively.

The initial states for each reaction pathway on each surface were chosen based on the configurations with the lowest adsorption energies. Fig. 6 shows the energy barriers for the considered reaction as determined by the NEB calculations. The configurations of ethanol on the surfaces at certain points of the reaction pathway are shown in the lower panel of Fig. 6. It can be seen that for the TiO₂ surface the initial state is 0.84 eV lower in energy than the final state where the hydrogen molecule detaches the surface, see Fig. 6a. Moreover, the determined energy barrier for this process is 2.25 eV. The rate-limiting step is step 2, where the first hydrogen atom is released from the ethanol.

For the (010)-WB_{5-x} surface the calculated energy barrier is shown in Fig. 6b. One can see that the final state is 0.93 eV higher than the initial state. The first hydrogen atom is released from ethanol on the (010)-WB_{5-x} surface in step 2 of Fig. 6b, which requires an energy of 0.62 eV. However, this is not the rate-limiting step, while it is step 3 which is associated with the release of the second hydrogen atom and subsequent formation of the H₂ molecule, see Fig. 6b. As a result, the activation energy for this process on the (010)-WB_{5-x} surface is 1.83 eV.

The second considered surface of WB_{5-x} shows an even lower activation barrier of 1.71 eV, see Fig. 6c. The rate-limiting process here is the release of the entire H₂ molecule from the ethanol adsorbed on the surface (step 2 in Fig. 6c). In contrast to the other two surfaces, the

energy of the final step is 0.36 eV lower than that of the initial step. This indicates that H₂ production from ethanol is more energetically favorable on this particular surface than on (010) or even TiO₂.

Obtained data on activation energies of H₂ generation from ethanol on the considered surfaces support our previous conclusions based on electronic structure calculations. Provided theoretical data explain the effectiveness of using WB_{5-x}-WB₂ as cocatalyst for TiO₂ catalyst in H₂ generation photocatalytic reaction.

3.4. Photocatalytic measurements

Composite WB_{5-x}-WB₂/TiO₂ photocatalysts, as well as unmodified samples of WB_{5-x}-WB₂ and commercial TiO₂, were tested for photocatalytic H₂ evolution and CO₂ reduction under visible light irradiation (410 nm). In both reactions, all composite photocatalysts showed higher activity than the unmodified precursors TiO₂ and WB_{5-x}-WB₂. The photocatalytic experiments were carried out three times, the variation was not more than 10 %. In the case of CO₂RR, blank experiments were performed in the absence of light, photocatalyst or CO₂, and in all cases no increase in CO or CH₄ in the reactor was detected by gas chromatography.

In the case of HER, the reaction rate increases with increasing WB_{5-x}-WB₂ content from 0 to 5 wt%, and the maximum activity is 81 μmol h⁻¹ g⁻¹, see Fig. 7a. We also observed that even 1 wt% of WB_{5-x}-WB₂ (which is not detectable by XRD) increases the activity several times compared to pure titanium dioxide (0 wt% WB_{5-x}-WB₂ in Fig. 7a). Further increase of the WB_{5-x}-WB₂ content up to 20 wt% does not lead to an increase in activity (Fig. 7a). This dependence with maximum reaction rate at optimum cocatalyst loading is typical for composite photocatalysts [37,76], since, on the one hand, an increase in the number of cocatalyst particles leads to an increase in the lifetime of the photogenerated charge carriers. On the other hand, a high concentration of cocatalyst particles usually prevents the adsorption of reagents and the absorption of light on the TiO₂ surface. Thus, the addition of 5 wt% of WB_{5-x}-WB₂ on the TiO₂ surface allowed us to prepare an optimal photocatalyst exhibiting the highest activity in HER among the synthesized samples, which is 23 times higher than that of pure TiO₂.

A similar behavior is also observed for the dependence of the rate of CO₂ reduction on the content of WB_{5-x}-WB₂ (Fig. 7d). The maximum activity is achieved on the 10 % WB_{5-x}-WB₂/TiO₂ photocatalyst and is 4 times higher than the activity of unmodified TiO₂ (Fig. 7d and S7). It can be concluded a high content (20 %) of cocatalyst screens a fairly large part of the TiO₂ surface and prevents the absorption of light and the adsorption of reagents. It is worth noting that the optimal amount of cocatalyst for the HER and CO₂RR is not coincide. Despite the fact that in both reactions the reducing agent is a photogenerated electron, the reactions of photocatalytic hydrogen evolution and carbon dioxide reduction have significant differences in the mechanisms. The main contribution to the rate of CO₂RR in terms of the total rate of consumption of photogenerated electrons is made by the eight-electron reduction of CO₂ to CH₄. The efficient occurrence of this process is possible only when a high electron density is achieved at the active center of the photocatalyst. This is accomplished, first of all, by the formation of heterojunctions of electrons from TiO₂ to a cocatalyst particle. Increasing the cocatalyst content results in more active centers with high electron density. This, in turn, increases the rate of CH₄ formation. Therefore, compared to the H₂ evolution, which requires only 2 electrons, the formation of CH₄ is a more complex process in terms of the formation rate and accumulation of electrons and requires more active centers with high electron density.

Since the photocatalytic reduction of CO₂ proceeds in the presence of water vapor, the process of H₂ formation can also occur in the reactor. Thus, three photocatalytic reactions can occur simultaneously: the reduction of CO₂ to CH₄ or CO, and the reduction of H⁺ to form H₂ (equations (3)–(5) [77]):

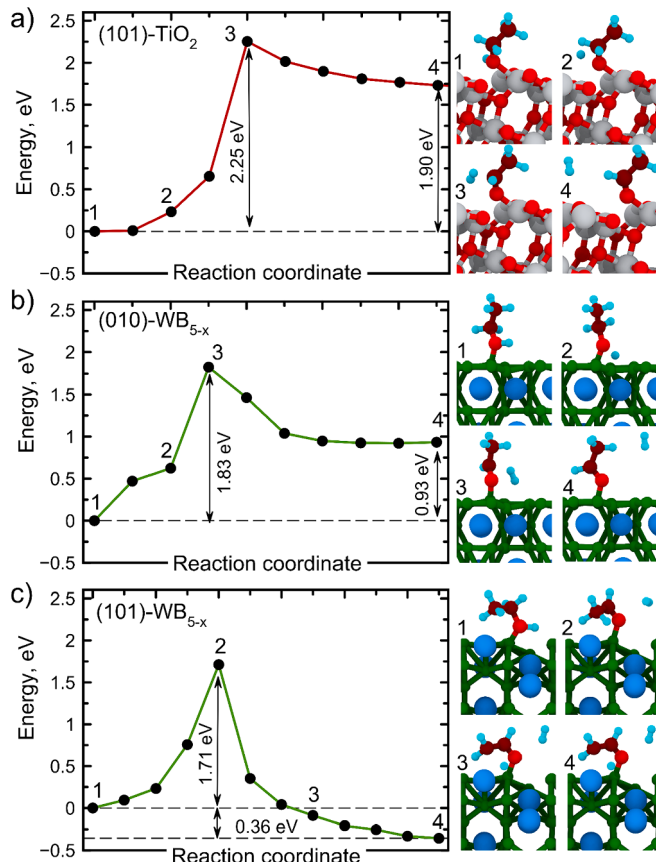


Fig. 6. Calculated energy barriers of desorption of H₂ molecule from the ethanol on the a) (101)-TiO₂, b) (010)-WB_{5-x}, and c) (101)-WB_{5-x} surfaces with selected atomic configurations shown in the right panels.

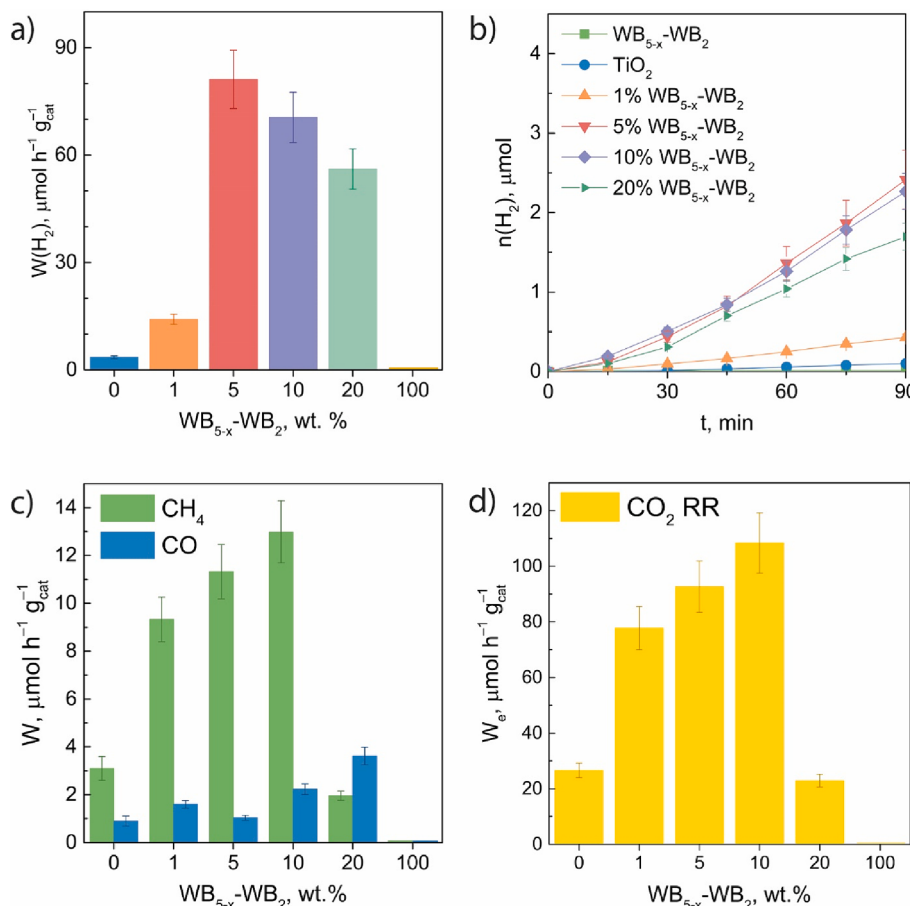
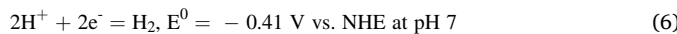
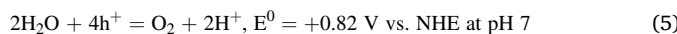
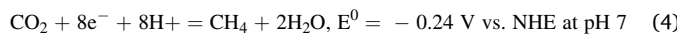
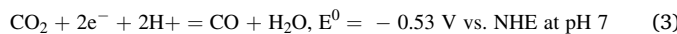


Fig. 7. A) activity in HER of TiO_2 , $\text{WB}_{5-x}\text{-WB}_2$, and (1–20 wt%) $\text{WB}_{5-x}\text{-WB}_2/\text{TiO}_2$. Conditions: $C(\text{cat.}) = 0.5 \text{ g L}^{-1}$, $C_0(\text{C}_2\text{H}_5\text{OH}) = 10 \text{ \%}$, $t(\text{reaction}) = 90 \text{ min}$, $\lambda = 410 \text{ nm}$ and b) H_2 evolution kinetics; c) CH_4 and CO formation rates and d) electron consumption rate for CO_2 reduction over TiO_2 , $\text{WB}_{5-x}\text{-WB}_2$, and (1–20 wt%) $\text{WB}_{5-x}\text{-WB}_2/\text{TiO}_2$. Conditions: $m(\text{cat.}) = 30 \text{ mg}$, $P_0(\text{CO}_2) = 1 \text{ atm}$, $t(\text{reaction}) = 4 \text{ h}$, $\lambda = 410 \text{ nm}$.



The calculation of the CO_2 reduction selectivity to CH_4 formation was carried out taking into account the electron balance according to the following formula:

$$S(\text{CH}_4), \% = (W(\text{CH}_4)/W_e(\text{CO}_2 \text{ RR})) 100 \% \quad (7)$$

where $W(\text{CO}_2 \text{ RR})$ is the rate of electron consumption for photocatalytic CO_2 reduction (eq. (1), $\mu\text{mol h}^{-1} \text{g}_{\text{cat}}^{-1}$; $W(\text{CH}_4)$ is the CH_4 evolution rate, $\mu\text{mol h}^{-1} \text{g}_{\text{cat}}^{-1}$.

Obtained results on the activity and selectivity of studied photocatalysts are summarized in **Table 2**. It can be seen that the rate of photocatalytic CO_2 reduction exceeds the rate of H_2 formation for all the studied materials. It should be noted that the 10 % $\text{WB}_{5-x}\text{-WB}_2/\text{TiO}_2$ photocatalyst has not only the highest rate of CO_2 reduction, but also the superior selectivity in this reaction. Regarding the process of CO_2 reduction, the composite photocatalysts mainly accelerate the reaction of CH_4 formation, while the rate of CO formation increases slightly compared to the unmodified TiO_2 . Thermodynamically, the process of reduction of CO_2 to methane is more favorable than the formation of CO . However, it requires 8 electrons, which makes CH_4 formation kinetically more difficult than the two-electron reduction process of CO_2 to CO .

Table 2

Measured activity and selectivity of studied photocatalysts of TiO_2 , $\text{WB}_{5-x}\text{-WB}_2$, and (1–20)% $\text{WB}_{5-x}\text{-WB}_2/\text{TiO}_2$.

| Photocatalyst | Product formation rate, $\mu\text{mol h}^{-1} \text{g}_{\text{cat}}^{-1}$ | | | $W_e(\text{CO}_2 \text{ RR}), \mu\text{mol h}^{-1} \text{g}_{\text{cat}}^{-1}$ | $S(\text{CH}_4), \%$ |
|------------------------------------|---|-------------|--------------|--|----------------------|
| | CH_4 | CO | H_2 | | |
| TiO_2 | 3.1 | 0.9 | 0.04 | 27 | 93.2 |
| $\text{WB}_{5-x}\text{-WB}_2$ | 0 | 0 | 0 | 0 | — |
| 1 % $\text{WB}_{5-x}\text{-WB}_2$ | 9.3 | 1.6 | 0.2 | 78 | 95.9 |
| 5 % $\text{WB}_{5-x}\text{-WB}_2$ | 11 | 1.0 | 0.2 | 93 | 97.8 |
| 10 % $\text{WB}_{5-x}\text{-WB}_2$ | 13 | 2.2 | 0.02 | 108 | 95.9 |
| 20 % $\text{WB}_{5-x}\text{-WB}_2$ | 2.0 | 3.6 | 0.02 | 23 | 69.0 |

Therefore, for the preferential reduction of CO_2 to methane, it is necessary to have a cocatalyst that can act as an effective trap for photogenerated electrons.

Based on electronic structure calculations, the following charge transfer scheme is realized in the synthesized photocatalysts. Under the light irradiation, electrons in TiO_2 jump from the valence band to the conduction band, thus forming electron-hole pairs. Due to the high recombination rate of the electrons and holes in unmodified TiO_2 , the lifetime of the photogenerated charge carriers is short and, therefore, the formation rate of CH_4 is low in this case. When WB_{5-x} particles are deposited on the surface of TiO_2 , heterotransfer of photogenerated electrons from the conduction band of TiO_2 to the Fermi level of the WB_{5-x} occurs in the contact sites TiO_2 and WB_{5-x} (**Fig. 8**). Thus, electrons accumulate on WB_{5-x} particles, which act as electron sinks, and spatial separation of photogenerated charges occurs. As the boride loading

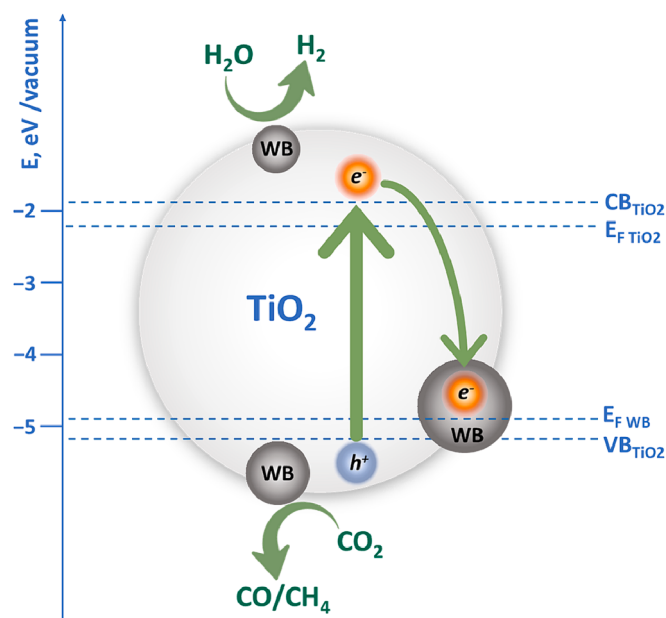


Fig. 8. Scheme of charge transfer mechanisms between TiO_2 and WB_{5-x} (WB) particles. $\text{CB}_{\text{TiO}2}$ – conduction band of TiO_2 , $\text{VB}_{\text{TiO}2}$ – valence band of TiO_2 , E_F TiO_2 and E_F WB – Fermi levels of TiO_2 and WB_{5-x} , respectively.

increases, there is also an increase in the number of TiO_2 - WB_{5-x} contact sites at which charge heterotransfer takes place. However, since WB_{5-x} is not a semiconductor, and its band structure is more similar to that of metals, light absorption leading to the formation of electron-hole pairs occurs on TiO_2 particles. Therefore, increasing the WB_{5-x} content leads to shielding of the TiO_2 surface and prevents the absorption of light by TiO_2 . Thus, an increase in WB_{5-x} loading has both a positive and negative effect on the efficiency of photocatalytic processes, so the dependence of the reaction rate on the WB_{5-x} content has a maximum at the point where the cocatalyst loading is optimal. It is worth emphasizing the deep location of the Fermi level of the WB_{5-x} , the value of which is comparable to the location of the Fermi level of the platinum (≈ -5.9 eV) [78]. Because of its band structure, WB_{5-x} can act as an effective electron trap, and depositing its particles on the surface of a semiconductor such as TiO_2 significantly increases the lifetime of photogenerated charge carriers and, consequently, photocatalytic activity.

4. Conclusions

In conclusion, a comprehensive experimental and computational study was carried out to propose a new extremely effective composite WB_{5-x} - WB_2 / TiO_2 photocatalyst for H_2 generation from ethanol aqueous solutions and CO_2 reduction under visible light irradiation (410 nm). WB_{5-x} - WB_2 powder was synthesized by vacuumless arc plasma technique and then mixed with TiO_2 substrate. We investigated photocatalysts containing 1, 5, 10, and 20 wt% of WB_{5-x} - WB_2 on TiO_2 and found that the optimal amount of cocatalyst to increase the reaction yield of H_2 generation several times is 5 wt%, the photocatalytic activity in this case is $81 \mu\text{mol h}^{-1} \text{g}_{\text{cat}}^{-1}$. To increase the rate of CH_4 and CO formation and CO_2 reduction reaction the 10 wt% of WB_{5-x} - WB_2 is the optimal amount, the maximum electron consumption rate for CO_2 reduction is $108 \mu\text{mol h}^{-1} \text{g}_{\text{cat}}^{-1}$. Further increases in the amount of cocatalyst do not improve the activity and selectivity of our composite photocatalyst. WB_{5-x} has been shown to be an effective alternative to platinum cocatalysts in photocatalytic applications due to its energy structure. The significance of the results extends far beyond the examined reactions. Our study presents a new application direction for transition metal borides as effective cocatalysts in photocatalytic reactions. This application is not limited to H_2 production and CO_2

reduction, but can be extended to many other reactions.

Author contributions

A.G.K., E.A.K. have initiated the project, P.V.P., A.Y.P. performed synthesis of powders of higher tungsten borides, V.S.B., A.D.R., A.G.K. performed theoretical calculations and analysis of obtained results. A.V. Z., A.Y.K., and E.A.K. did the experiments on the preparation of the composite photocatalyst, all measurements of reaction rates, yields etc. E.E.A., E.Y.G., and D.D.M. did the experiments on the characterization of the photocatalyst and analyzed the data obtained, V.S.B., A.G.K., A.Y.K., E.A.K. wrote the original draft of the manuscript. All the authors provided critical feedback and helped shape the research. The manuscript has been written through contributions of all authors. All the authors provided critical feedback and helped shape the research. All the authors have given approval to the final version of the manuscript.

CRediT authorship contribution statement

Anna Yu. Kurenkova: Writing – original draft, Visualization, Methodology, Investigation, Formal analysis, Data curation. **Aleksandra D. Radina:** Writing – original draft, Methodology, Investigation, Formal analysis, Data curation. **Viktor S. Baidyshev:** Methodology, Investigation, Formal analysis, Data curation. **Pavel V. Povalyaev:** Methodology, Investigation, Formal analysis, Data curation. **Egor E. Aidakov:** Visualization, Methodology, Investigation, Formal analysis, Data curation. **Evgeny Yu. Gerasimov:** Methodology, Investigation, Formal analysis, Data curation. **Denis D. Mishchenko:** Methodology, Investigation, Formal analysis, Data curation. **Angelina V. Zhurenok:** Methodology, Investigation, Formal analysis, Data curation. **Alexander Ya. Pak:** Supervision, Project administration, Formal analysis, Data curation. **Ekaterina A. Kozlova:** Project administration, Methodology, Investigation, Formal analysis, Conceptualization. **Alexander G. Kvashnin:** Writing – review & editing, Writing – original draft, Supervision, Software, Project administration, Methodology, Investigation, Data curation, Conceptualization.

Declaration of competing interest

The authors declare the following financial interests/personal relationships which may be considered as potential competing interests: [Alexander Pak reports financial support was provided by Ministry of Science Higher Education of the Russian Federation. If there are other authors, they declare that they have no known competing financial interests or personal relationships that could have appeared to influence the work reported in this paper.]

Data availability

Data will be made available on request.

Acknowledgements

A.Y.P and P.V.P. acknowledge support from the Ministry of Science Higher Education of the Russian Federation in part of the Science program (Project FSWW-2022-0018) for performing the vacuumless synthesis of higher tungsten boride. Authors thank the Tomsk Polytechnic University development program (DC arc plasma reactor system automation). A.Y.K., A.V.Z., and E.Y.G. thank the Russian Science Foundation for financial support of the experiments on CO_2 reduction and photocatalyst characterization by HRTEM (grant # 21-73-10235). The XPS and XRD experiments were performed using the facilities of the shared research center “National Center of Investigation of Catalysts” at Boreskov Institute of Catalysis.

Appendix A. Supplementary material

Supplementary data to this article can be found online at <https://doi.org/10.1016/j.apsusc.2024.160095>.

References

- [1] S. Linic, P. Christopher, D.B. Ingram, Plasmonic-metal nanostructures for efficient conversion of solar to chemical energy, *Nat. Mater.* 10 (2011) 911–921, <https://doi.org/10.1038/nmat3151>.
- [2] S. Mishra, R. Acharya, Recent updates in modification strategies for escalated performance of Graphene/MFe₂O₄ heterostructured photocatalysts towards energy and environmental applications, *J. Alloy. Compd.* 960 (2023) 170576, <https://doi.org/10.1016/j.jallcom.2023.170576>.
- [3] A. Chawla, A. Sudhaik, P. Soni, T. Raizada, Q.V. Ahamad, V.-H. Le, S. Nguyen, A. K. Thakur, R. Mishra, P.S. Selvasembian, Bi-rich BixOyBrz-based photocatalysts for energy conversion and environmental remediation: a review, *Coord. Chem. Rev.* 491 (2023) 215246, <https://doi.org/10.1016/j.ccr.2023.215246>.
- [4] X. Yang, D. Wang, Photocatalysis: from fundamental principles to materials and applications, *ACS Appl. Energy Mater.* 1 (2018) 6657–6693, <https://doi.org/10.1021/acsaem.8b01345>.
- [5] Z. Xiong, Z. Lei, Y. Li, L. Dong, Y. Zhao, J. Zhang, A review on modification of facet-engineered TiO₂ for photocatalytic CO₂ reduction, *J. Photochem. Photobiol. C: Photochem. Rev.* 36 (2018) 24–47, <https://doi.org/10.1016/j.jphotochemrev.2018.07.002>.
- [6] M. Zhou, Z. Wang, A. Mei, Z. Yang, W. Chen, S. Ou, S. Wang, K. Chen, P. Reiss, K. Qi, J. Ma, Y. Liu, Photocatalytic CO₂ reduction using la-ni bimetallic sites within a covalent organic framework, *Nat. Commun.* 14 (2023) 2473, <https://doi.org/10.1038/s41467-023-37545-2>.
- [7] J. Albero, Y. Peng, H. García, Photocatalytic CO₂ reduction to C₂₊ products, *ACS Catal.* 10 (2020) 5734–5749, <https://doi.org/10.1021/acscatal.0c00478>.
- [8] L. Liao, G. Xie, X. Xie, N. Zhang, Advances in modulating the activity and selectivity of photocatalytic CO₂ reduction to Multicarbon products, *J. Phys. Chem. C* 127 (2023) 2766–2781, <https://doi.org/10.1021/acs.jpcc.2c08963>.
- [9] M. Duflot, C. Marchal, V. Caps, V. Artero, K. Christoforidis, V. Keller, Optimization of NH2-Uio-66/TiO₂/Au composites for enhanced gas-phase CO₂ photocatalytic reduction into CH₄, *Catal. Today* 413–415 (2023) 114018, <https://doi.org/10.1016/j.cattod.2023.01.025>.
- [10] R.-T. Guo, Z.-R. Zhang, C. Xia, C.-F. Li, W.-G. Pan, Recent progress of cocatalysts loaded on carbon nitride for selective photoreduction of CO₂ to CH₄, *Nanoscale* 15 (2023) 8548–8577, <https://doi.org/10.1039/D3NR00242J>.
- [11] Y. Liu, Z. Sun, Y.H. Hu, Bimetallic cocatalysts for photocatalytic hydrogen production from water, *Chem. Eng. J.* 409 (2021) 128250, <https://doi.org/10.1016/j.cej.2020.128250>.
- [12] K.C. Christoforidis, P. Fornasier, Photocatalytic hydrogen production: a rift into the future energy supply, *ChemCatChem* 9 (2017) 1523–1544, <https://doi.org/10.1002/cctc.201601659>.
- [13] S. Wang, Y. Hou, X. Wang, Development of a stable MnCo₂O₄ cocatalyst for photocatalytic CO₂ reduction with visible light, *ACS Appl. Mater. Interfaces* 7 (2015) 4327–4335, <https://doi.org/10.1021/am508766s>.
- [14] D.I. Kondarides, V.M. Dascalaki, A. Patsoura, X.E. Verykios, Hydrogen production by photo-induced reforming of biomass components and derivatives at ambient conditions, *Catal Lett* 122 (2008) 26–32, <https://doi.org/10.1007/s10562-007-9330-3>.
- [15] M. Tahir, S. Tasleem, B. Tahir, Recent development in band engineering of binary semiconductor materials for solar driven photocatalytic hydrogen production, *Int. J. Hydrogen Energy* 45 (2020) 15985–16038, <https://doi.org/10.1016/j.ijhydene.2020.04.071>.
- [16] V. Preethi, S. Kanmani, Photocatalytic hydrogen production, *Mater. Sci. Semicond. Process.* 16 (2013) 561–575, <https://doi.org/10.1016/j.msspp.2013.02.001>.
- [17] M.R. Karimi Estebanabati, A. Babin, M. Feilizadeh, Z. Nayernia, N. Mahinpey, M. C. Iliuta, Photocatalytic conversion of alcohols to hydrogen and carbon-containing products: a cleaner alcohol valorization approach, *J. Clean. Prod.* 318 (2021) 128546, <https://doi.org/10.1016/j.jclepro.2021.128546>.
- [18] A. Fujishima, X. Zhang, D.A. Tryk, TiO₂ photocatalysis and related surface phenomena, *Surf. Sci. Rep.* 63 (2008) 515–582, <https://doi.org/10.1016/j.surfrep.2008.10.001>.
- [19] M. Ismael, A review and recent advances in solar-to-hydrogen energy conversion based on photocatalytic water splitting over doped-TiO₂ nanoparticles, *Sol. Energy* 211 (2020) 522–546, <https://doi.org/10.1016/j.solener.2020.09.073>.
- [20] D.Y.C. Leung, X. Fu, C. Wang, M. Ni, M.K.H. Leung, X. Wang, X. Fu, Hydrogen production over titania-based photocatalysts, *ChemSusChem* 3 (2010) 681–694, <https://doi.org/10.1002/cssc.201000014>.
- [21] A. Naldoni, M. Altomare, G. Zopellaro, N. Liu, Š. Kment, R. Zboril, P. Schmuki, Photocatalysis with reduced TiO₂: from black TiO₂ to cocatalyst-free hydrogen production, *ACS Catal.* 9 (2019) 345–364, <https://doi.org/10.1021/acscatal.8b04068>.
- [22] X. Chen, R. Guo, L. Hong, Y. Yuan, W. Pan, Research Progress on CO₂ photocatalytic reduction with full Solar spectral responses, *Energy Fuels* 35 (2021) 19920–19942, <https://doi.org/10.1021/acs.energyfuels.1c03374>.
- [23] P. Gomatisankar, D. Yamamoto, H. Katsumata, T. Suzuki, S. Kaneko, Photocatalytic hydrogen production with aid of simultaneous metal deposition using titanium dioxide from aqueous glucose solution, *Int. J. Hydrogen Energy* 38 (2013) 5517–5524, <https://doi.org/10.1016/j.ijhydene.2013.03.014>.
- [24] Z. Lin, S.R. Denny, J.G. Chen, Transition metal carbides and nitrides as catalysts for thermochemical reactions, *J. Catal.* 404 (2021) 929–942, <https://doi.org/10.1016/j.jcat.2021.06.022>.
- [25] H. Zhang, X. Yang, H. Zhang, J. Ma, Z. Huang, J. Li, Y. Wang, Transition-metal Carbides as hydrogen evolution reduction electrocatalysts: synthetic methods and optimization strategies, *Chem. – a Europ. J.* 27 (2021) 5074–5090, <https://doi.org/10.1002/chem.202003979>.
- [26] M. Lewandowski, M. Bartoszewicz, K. Jaroszewska, G. Djéga-Mariadassou, Transition metal borides of ni-B (co-B) as alternative non-precious catalytic materials: advances, potentials, and challenges. short review, *J. Ind. Eng. Chem.* 116 (2022) 75–98, <https://doi.org/10.1016/j.jiec.2022.09.031>.
- [27] E. Lee, H. Park, H. Joo, B.P.T. Fokwa, Unexpected Correlation between boron chain condensation and hydrogen evolution reaction (HER) activity in highly active vanadium borides: enabling predictions, *Angew. Chem. Int. Ed.* 59 (2020) 11774–11778, <https://doi.org/10.1002/anie.202000154>.
- [28] L. Cui, W. Zhang, R. Zheng, J. Liu, Electrocatalysts based on transition metal borides and borates for the oxygen evolution reaction, *chemistry – a European Journal* 26 (2020) 11661–11672, <https://doi.org/10.1002/chem.202000880>.
- [29] Q. Li, L. Wang, X. Ai, H. Chen, J. Zou, G.-D. Li, X. Zou, Multiple crystal phases of intermetallic tungsten borides and phase-dependent electrocatalytic property for hydrogen evolution, *Chem. Commun.* 56 (2020) 13983–13986, <https://doi.org/10.1039/D0CC06072K>.
- [30] S. Gupta, M.K. Patel, A. Miello, N. Patel, Metal boride-based catalysts for electrochemical water-splitting: a review, *Adv. Funct. Mater.* (2020) 1906481, <https://doi.org/10.1002/adfm.201906481>.
- [31] Z. Zhang, Z.-H. Cui, E. Jimenez-Izal, P. Sautet, A.N. Alexandrova, Hydrogen evolution on restructured B-rich WB: metastable Surface states and isolated active sites, *ACS Catal.* (2020) 13867–13877, <https://doi.org/10.1021/acscatal.0c03410>.
- [32] Y. Li, T. Chao, X. Luo, W. Chen, B. Jiang, J. Ge, Y. Lin, G. Wu, X. Wang, Y. Hu, Z. Zhuang, Y. Wu, X. Hong, Atomically dispersed cu-pt dual sites alloyed pd nanorings for hydrogen evolution reaction, andewandte, *Chemie* 56 (2017) 16047–16051, <https://doi.org/10.1002/ange.201709803>.
- [33] J. Sun, X. Zhang, M. Jin, Q. Xiong, G. Wang, H. Zhang, H. Zhao, Robust enhanced hydrogen production at acidic conditions over molybdenum oxides-stabilized ultrafine palladium electrocatalysts, *Nano Res.* 14 (2021) 268–274, <https://doi.org/10.1007/s12274-020-3083-3>.
- [34] G.P. Shveikin, A.L. Ivanovskii, The chemical bonding and electronic properties of metal borides, *Russ. Chem. Rev.* 63 (1994) 711, <https://doi.org/10.1070/RC1994v06n09ABEH000114>.
- [35] V. Kumaravel, J. Bartlett, S.C. Pillai, Photoelectrochemical conversion of Carbon dioxide (CO₂) into fuels and value-added products, *ACS Energy Lett.* (2020) 486–519, <https://doi.org/10.1021/acsenergylett.9b02585>.
- [36] A.A. Saraev, A.Y. Kurenkova, A.V. Zhurenok, E.Y. Gerasimov, E.A. Kozlova, Selectivity control of CO₂ reduction over Pt/g-C₃N₄ photocatalysts under visible light, *Catalysts* 13 (2023) 273, <https://doi.org/10.3390/catal13020273>.
- [37] P. Tkachenko, V. Volchek, A. Kurenkova, E. Gerasimov, P. Popovetskiy, I. Asanov, I. Yushina, E. Kozlova, D. Vasilchenko, Photocatalytic H₂ generation from ethanol and glucose aqueous solutions by PtO_x/TiO₂ composites, *Int. J. Hydrogen Energy* (2022), <https://doi.org/10.1016/j.ijhydene.2022.11.265>.
- [38] T. Hou, S. Zhang, Y. Chen, D. Wang, W. Cai, Hydrogen production from ethanol reforming: catalysts and reaction mechanism, *Renew. Sustain. Energy Rev.* 44 (2015) 132–148, <https://doi.org/10.1016/j.rser.2014.12.023>.
- [39] A.Y. Pak, D.V. Rybkovsky, Y.Z. Vassilyeva, E.N. Kolobova, A.V. Filimonenko, A.G. Kvashnin, Efficient synthesis of WB_{5-x}–WB₂ powders with selectivity for WB_{5-x} content, *Inorg. Chem.* 61 (2022) 6773–6784, <https://doi.org/10.1021/acs.inorgchem.1c03880>.
- [40] A.Y. Pak, V. Sotskov, A.G. Gumovskaya, Y.Z. Vassilyeva, Z.S. Bolatova, Y.A. Kvashnina, G.Y. Mamontov, A.V. Shapeev, A.G. Kvashnin, Machine learning-driven synthesis of Ti₂ZrNbHfTaC₅ high-entropy carbide, *Npj Comput Mater* 9 (2023) 1–11, <https://doi.org/10.1038/s41524-022-00955-9>.
- [41] B.H. Toby, R.B. Von Dreele, GSAS-II: the genesis of a modern open-source all purpose crystallography software package, *J Appl Cryst* 46 (2013) 544–549, <https://doi.org/10.1107/S0021889813003531>.
- [42] A.A. Saraev, A.Y. Kurenkova, E.Y. Gerasimov, E.A. Kozlova, Broadening the action Spectrum of TiO₂-based photocatalysts to visible region by substituting platinum with copper, *Nanomaterials* 9 (2022) 1584, <https://doi.org/10.3390/nano12091584>.
- [43] A.H. Larsen, J.J. Mortensten, J. Blomqvist, I.E. Castelli, R. Christensen, M. Dulak, J. Friis, M.N. Groves, B. Hammer, C. Hargas, E.D. Hermes, P.C. Jennings, P.B. Jensen, J. Kermode, J.R. Kitchin, E.L. Kolsbjerg, J. Kubal, K. Kaasbjerg, S. Lysgaard, J. Bergmann Marosson, T. Maxson, T. Olsen, L. Pastewka, A. Peterson, C. Rostgaard, J. Schiotz, O. Schutt, M. Strange, K.S. Thygesen, T. Vegge, L. Vilhelmsen, M. Walter, Z. Zeng, K.W. Jacobsen, The atomic simulation environment — A python library for working with atoms, *J. Phys. Condens. Matter* 29 (2017) 273002, <https://doi.org/10.1088/1361-648X/aa680e>.
- [44] A.G. Kvashnin, D.V. Rybkovsky, V.P. Filonenko, V.I. Bugakov, I.P. Zibrov, V.V. Brazhkin, A.R. Oganov, A.A. Osipov, A.Y. Zakirov, WB_{5-x}: synthesis, properties, and crystal structure—New insights into the long-debated compound, *advanced, Science* (2020) 2000775, <https://doi.org/10.1002/advs.202000775>.
- [45] A. Jain, S.P. Ong, G. Hautier, W. Chen, W.D. Richards, S. Dacek, S. Cholia, D. Gunter, D. Skinner, G. Ceder, K.A. Persson, Commentary: the materials project: a materials genome approach to accelerating materials innovation, *APL Mater.* 1 (2013) 011002, <https://doi.org/10.1063/1.4812323>.
- [46] K. Bourikas, C. Kordulis, A. Lycurghiotis, Titanium dioxide (anatase and rutile): Surface chemistry, liquid-solid Interface chemistry, and scientific synthesis of

- supported catalysts, Chem. Rev. 114 (2014) 9754–9823, <https://doi.org/10.1021/cr300230q>.
- [47] G. Kresse, J. Furthmüller, Efficient iterative schemes for ab initio total-energy calculations using a plane-wave basis set, Phys. Rev. B, Condensed Matter 16 (1996) 11169–11186, <https://doi.org/10.1103/physrevb.54.11169>.
- [48] G.A. de Wijs, P.K. de Boer, R.A. de Groot, G. Kresse, Anomalous behavior of the semiconducting gap in WO_3 from first-principles calculations, Phys. Rev. B, Condensed Matter 59 (1999) 2684–2693, <https://doi.org/10.1103/PhysRevB.59.2684>.
- [49] G. Kresse, J. Furthmüller, Efficiency of ab-initio total energy calculations for metals and semiconductors using a plane-wave basis set, Comput. Mater. Sci. 6 (1996) 15–50, [https://doi.org/10.1016/0927-0256\(96\)00008-0](https://doi.org/10.1016/0927-0256(96)00008-0).
- [50] J.P. Perdew, K. Burke, Y. Wang, Generalized gradient approximation for the exchange-correlation hole of a many-electron system, Phys. Rev. B, Condensed Matter 54 (1996) 16533–16539, <https://doi.org/10.1103/physrevb.54.16533>.
- [51] G. Kresse, D. Joubert, From ultrasoft pseudopotentials to the projector augmented-wave method, Phys. Rev. B, Condensed Matter 59 (1999) 1758–1775, <https://doi.org/10.1103/PhysRevB.59.1758>.
- [52] H.J. Monkhorst, J.D. Pack, Special points for brillouin-zone integrations, Phys. Rev. B 13 (1976) 5188–5192, <https://doi.org/10.1103/PhysRevB.13.5188>.
- [53] V.I. Anisimov, J. Zaanen, O.K. Andersen, Band theory and Mott insulators: Hubbard U instead of stoner I, Phys. Rev. B 44 (1991) 943–954, <https://doi.org/10.1103/PhysRevB.44.943>.
- [54] S.L. Dudarev, G.A. Botton, S.Y. Savrasov, C.J. Humphreys, A.P. Sutton, Electron-energy-loss spectra and the structural stability of nickel oxide: an LSDA+U study, Phys. Rev. B 57 (1998) 1505–1509, <https://doi.org/10.1103/PhysRevB.57.1505>.
- [55] A. Bartkowiak, O. Korolevych, G.L. Chiarello, M. Makowska-Janusik, M. Zalas, How can the introduction of Zr^{4+} ions into TiO_2 nanomaterial impact the DSSC photoconversion efficiency? a comprehensive theoretical and experimental consideration, Materials 14 (2021) 2955, <https://doi.org/10.3390/ma14112955>.
- [56] T. Luttrell, S. Halpegamage, J. Tao, A. Kramer, E. Sutter, M. Batzill, Why is anatase a better photocatalyst than rutile? - model studies on epitaxial TiO_2 films, Sci. Rep. 4 (2014) 4043, <https://doi.org/10.1038/srep04043>.
- [57] S. Grimme, J. Antony, S. Ehrlich, H. Krieg, A consistent and accurate ab initio parametrization of density functional dispersion correction (DFT-D) for the 94 elements H-pu, J. Chem. Phys. 132 (2010) 154104, <https://doi.org/10.1063/1.3382344>.
- [58] G. Henkelman, B.P. Uberuaga, H. Jonsson, A climbing image nudged elastic band method for finding saddle points and minimum energy paths, J. Chem. Phys. 113 (2000) 9901, <https://doi.org/10.1063/1.1329672>.
- [59] Y.P. Xie, G. Liu, G.Q. (Max) Lu, H.-M. Cheng, Boron oxynitride nanoclusters on tungsten trioxide as a metal-free cocatalyst for photocatalytic oxygen evolution from water splitting, Nanoscale 4 (2012) 1267–1270. doi: 10.1039/C2NR11846G.
- [60] Z. Wu, Y. Long, H.-T. Lin, F. Zhang, Effect of tantalum on phase transition and thermal stability of metastable tungsten tetra-boride, Ceram. Int. 46 (2020) 17217–17223, <https://doi.org/10.1016/j.ceramint.2020.03.294>.
- [61] T. Moscicki, R. Psiuk, H. Stomirska, N. Leviant-Zayonts, D. Garbiec, M. Pisarek, P. Bazarnik, S. Nosewicz, J. Chrzanowska-Giżyńska, Influence of overstoichiometric boron and titanium addition on the properties of RF magnetron sputtered tungsten borides, Surf. Coat. Technol. 390 (2020) 125689, <https://doi.org/10.1016/j.surcoa.2020.125689>.
- [62] J. Chrzanowska-Giżyńska, P. Denis, S. Woźniacka, Ł. Kurpaska, Mechanical properties and thermal stability of tungsten boride films deposited by radio frequency magnetron sputtering, Ceram. Int. 44 (2018) 19603–19611, <https://doi.org/10.1016/j.ceramint.2018.07.208>.
- [63] A. Romanyuk, R. Steiner, L. Marot, P. Oelhafen, Temperature-induced metal-semiconductor transition in W-doped VO_2 films studied by photoelectron spectroscopy, Sol. Energy Mater. Sol. Cells 91 (2007) 1831–1835, <https://doi.org/10.1016/j.solmat.2007.06.013>.
- [64] B. Rubin, J.L. Topper, A.P. Yalin, Total and differential sputter yields of boron nitride measured by quartz crystal microbalance, J. Phys. D: Appl. Phys. 42 (2009) 205205, <https://doi.org/10.1088/0022-3727/42/20/205205>.
- [65] M.F. Genisel, M.N. Uddin, Z. Say, M. Kulakci, R. Turan, O. Gulseren, E. Bengu, Bias in bonding behavior among boron, carbon, and nitrogen atoms in ion implanted a-BN, a-BC, and diamond like carbon films, J. Appl. Phys. 110 (2011) 074906, <https://doi.org/10.1063/1.3638129>.
- [66] G. Puyou, F. Teyssandier, R. Pailler, C. Labrugère, G. Chollon, Boron carbonitride coatings synthesized by LPCVD, structure and properties, Carbon 122 (2017) 19–46, <https://doi.org/10.1016/j.carbon.2017.06.024>.
- [67] J. Jun, M. Dhayal, J.-H. Shin, J.-C. Kim, N. Getoff, Surface properties and photoactivity of TiO_2 treated with electron beam, Radiat. Phys. Chem. 75 (2006) 583–589, <https://doi.org/10.1016/j.radphyschem.2005.10.015>.
- [68] J. Liu, L. Han, N. An, L. Xing, H. Ma, L. Cheng, J. Yang, Q. Zhang, Enhanced visible-light photocatalytic activity of carbonate-doped anatase TiO_2 based on the electron-withdrawing bidentate carboxylate linkage, Appl. Catal. B 202 (2017) 642–652, <https://doi.org/10.1016/j.apcatb.2016.09.057>.
- [69] O.M. Moon, B.-C. Kang, S.-B. Lee, J.-H. Boo, Temperature effect on structural properties of boron oxide thin films deposited by MOCVD method, Thin Solid Films 464–465 (2004) 164–169, <https://doi.org/10.1016/j.tsf.2004.05.107>.
- [70] A. Nakao, M. Iwaki, H. Sakai, K. Terasima, XPS characterization of nitrogen implanted silicon carbide, Nucl. Instrum. Methods Phys. Res., Sect. B 65 (1992) 352–356, [https://doi.org/10.1016/0168-583X\(92\)95065-Y](https://doi.org/10.1016/0168-583X(92)95065-Y).
- [71] R. Machorro, E.C. Samano, G. Soto, L. Cota, SiCxNy thin films alloys prepared by pulsed excimer laser deposition, Appl. Surf. Sci. 127–129 (1998) 564–568, [https://doi.org/10.1016/S0169-4332\(97\)00706-X](https://doi.org/10.1016/S0169-4332(97)00706-X).
- [72] C.V. Ramana, R.S. Vemuri, V.V. Kaichev, V.A. Kochubey, A.A. Saraev, V. V. Atuchin, X-ray photoelectron spectroscopy depth profiling of $\text{La}_2\text{O}_3/\text{Si}$ thin films deposited by reactive magnetron sputtering, ACS Appl. Mater. Interfaces 3 (2011) 4370–4373, <https://doi.org/10.1021/am201021m>.
- [73] D. Bociaga, A. Sobczyk-Guzenda, P. Komorowski, J. Balcerzak, K. Jastrzebski, K. Przybyszewska, A. Kaczmarek, Surface Characteristics and biological evaluation of si-DLC coatings fabricated using magnetron sputtering method on $\text{Ti}_6\text{Al}_7\text{Nb}$ substrate, Nanomaterials 9 (2019) 812, <https://doi.org/10.3390/nano9060812>.
- [74] E. Bengu, M.F. Genisel, O. Gulseren, R. Ovali, Theoretical and spectroscopic investigations on the structure and bonding in B-C-N thin films, Thin Solid Films 518 (2009) 1459–1464, <https://doi.org/10.1016/j.tsf.2009.09.106>.
- [75] A.Y. Kurenkova, A.M. Kremneva, A.A. Saraev, V. Murzin, E.A. Kozlova, V. V. Kaichev, Influence of thermal activation of titania on photoreactivity of Pt/ TiO_2 in hydrogen production, Catal. Lett. 151 (2021) 748–754, <https://doi.org/10.1007/s10562-020-03321-w>.
- [76] A.A. Saraev, A.Y. Kurenkova, D.D. Mishchenko, A.L. Trigub, E.Y. Gerasimov, E. A. Kozlova, Cu/ TiO_2 photocatalysts for CO₂ reduction: structure and evolution of the cocatalyst active form, Trans. Tianjin Univ. (2024), <https://doi.org/10.1007/s12209-024-00384-3>.
- [77] A.M. Sadanandan, J.-H. Yang, V. Devtade, G. Singh, N. Panangattu Dharmarajan, M. Fawaz, J. Mee Lee, E. Tavakkoli, C.-H. Jeon, P. Kumar, A. Vinu, Carbon nitride based nanoarchitectonics for nature-inspired photocatalytic CO₂ reduction, Prog. Mater Sci. 142 (2024) 101242, <https://doi.org/10.1016/j.jpmatsci.2024.101242>.
- [78] J. Kaur, R. Singh, B. Pal, Influence of coinage and platinum group metal co-catalysis for the photocatalytic reduction of *m*-dinitrobenzene by P25 and rutile TiO_2 , J. Mol. Catal. A Chem. 397 (2015) 99–105, <https://doi.org/10.1016/j.molcata.2014.11.007>.